



HAL
open science

Gas barrier properties of polylactide/cellulose nanocrystals nanocomposites

Hajar Faraj, Nadège Follain, Cyrille Sollogoub, Giana Almeida, Corinne Chappey, Stéphane Marais, Sylvie Tencé-Girault, Fabrice Gouanvé, Eliane Espuche, Sandra Domenek

► **To cite this version:**

Hajar Faraj, Nadège Follain, Cyrille Sollogoub, Giana Almeida, Corinne Chappey, et al.. Gas barrier properties of polylactide/cellulose nanocrystals nanocomposites. *Polymer Testing*, 2022, 113, pp.107683. 10.1016/j.polymertesting.2022.107683 . hal-03794868

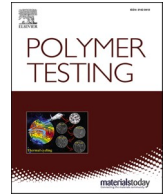
HAL Id: hal-03794868

<https://hal.science/hal-03794868>

Submitted on 3 Oct 2022

HAL is a multi-disciplinary open access archive for the deposit and dissemination of scientific research documents, whether they are published or not. The documents may come from teaching and research institutions in France or abroad, or from public or private research centers.

L'archive ouverte pluridisciplinaire **HAL**, est destinée au dépôt et à la diffusion de documents scientifiques de niveau recherche, publiés ou non, émanant des établissements d'enseignement et de recherche français ou étrangers, des laboratoires publics ou privés.



Gas barrier properties of polylactide/cellulose nanocrystals nanocomposites

Hajar Faraj^{a,b}, Nadège Follain^c, Cyrille Sollogoub^b, Giana Almeida^a, Corinne Chappey^c, Stéphane Marais^c, Sylvie Tencé-Girault^b, Fabrice Gouanvé^d, Eliane Espuche^d, Sandra Domenek^{a,*}

^a Université Paris-Saclay, INRAE, AgroParisTech, UMR SayFood, 91300, Massy, France

^b Laboratoire PIMM, Arts et Metiers Institute of Technology, CNRS, Cnam, Hesam Université, 151, Boulevard de l'Hopital, 75013, Paris, France

^c Normandie University, UNIROUEN, INSA Rouen, CNRS, PBS, 76000, Rouen, France

^d Université Lyon 1, CNRS UMR 5223, Ingénierie des Matériaux Polymères, 69622, Villeurbanne, France

ARTICLE INFO

Keywords:

PLA
CNC
Nanocomposites
Gas barrier properties
Nielsen model
Biocomposites
polylactic acid

ABSTRACT

The development of polylactide (PLA)/cellulose nanocrystals (CNC) nanocomposites in the aim to increase gas barrier properties has been widely studied, but gave rise to conflicting results. To better understand the underlying gas transport mechanisms, PLA/CNC nanocomposites were produced at concentrations between 5 and 50 wt%. The role of the PLA/CNC interface for the permeability was investigated using three different CNC surface grafts, namely lauric acid (slightly interacting with PLA), stearic acid (non-interacting with PLA), and poly glycidyl methacrylate bearing a reactive epoxy end-group (crosslinking with PLA). While PLA/CNC composites contained a large number of aggregates, homogeneously dispersed nanocomposites were obtained with surface modified CNCs even at high concentration of CNC (up to 30 wt%). All nanocomposites had better O₂ and CO₂ barrier properties than PLA. Surprisingly, the nanocomposites prepared with surface grafted CNC did not perform better than the ones prepared with neat CNC. The diffusion coefficient was successfully modeled with Nielsen's law, showing the importance of the shape factor and resulting tortuosity for the barrier performance notwithstanding PLA/CNC surface compatibility. The analysis of the dual-mode O₂ sorption isotherm showed the creation of a similar quantity of supplementary sorption sites in nanocomposites prepared with neat or lauric acid grafted CNC. PGMA grafts induced a higher number of sorption sites. The most important advantage of CNC surface grafts was the shielding of CNC against water vapor uptake. As a result, the O₂ barrier properties could be maintained constant up to 90% relative humidity.

1. Introduction

Gas barrier properties are of high importance in many fields, in particular barrier properties to O₂, CO₂ and H₂O are required in many food packaging applications to preserve the food quality. Polylactide (PLA) and cellulose nanocrystals (CNC) are of great interest, because both components present an attractive biobased and biodegradable alternative to petroleum-based polymers for packaging applications [1–4]. Nanocellulose films show excellent O₂ barrier properties ($\sim 10^{-21} \text{ m}^3 \text{ mm}^{-2} \text{ s}^{-1} \cdot \text{Pa}^{-1}$), which are under dry conditions equal or even better than the widely used polymer ethyl vinyl alcohol (EVOH) [5–7]. This can be attributed to their crystallinity and high polarity [8]. CNCs are highly hydrophilic, due to their chemical nature and the high

concentration of hydroxyl groups on their surface [9]. Therefore, they exhibit a very low moisture resistance and quickly lose performance when the relative humidity is higher than 60% [6]. PLA is known for its limited barrier properties to gases (such as dioxygen and carbon dioxide) but is more hydrophobic than CNC. PLA/CNC composites could thus improve on the one hand O₂ and CO₂ barrier properties because CNCs are impermeable obstacles for gas diffusion and on the other hand PLA could act as a protection of the CNCs from humidity.

Recent theoretical results in modeling of mass transfer in nanocomposites show that the rod-like shape of CNC induces the need for high concentration if a notable effect on barrier properties is targeted. Typically, a decrease by a factor 2 of the diffusion coefficient would need at least 30 vol% of a monodispersed filler with an aspect ratio of 5 [10].

* Corresponding author. UMR SayFood, 91300, Massy, France.

E-mail address: sandra.domenek@agroparistech.fr (S. Domenek).

<https://doi.org/10.1016/j.polymeresting.2022.107683>

Received 31 March 2022; Received in revised form 14 June 2022; Accepted 25 June 2022

Available online 1 July 2022

0142-9418/© 2022 The Authors. Published by Elsevier Ltd. This is an open access article under the CC BY-NC-ND license (<http://creativecommons.org/licenses/by-nc-nd/4.0/>).

The combination of these two components is however challenging, because the inherent chemical compatibility between hydrophobic PLA and hydrophilic CNC is low. A consequence is a poor dispersion of CNC inside the polymer, limiting or reducing the final properties of the composite material. Moreover, poor matrix/filler adhesion can generate cavities at the interface, or a decrease in polymer density in vicinity of interfaces. Both phenomena create more free volume and are detrimental for barrier properties. Today, only few reported studies on the compatibilization of PLA/CNC nanocomposites focus on the barrier properties [11–15]. Different strategies of CNC surface compatibilization or modification, either by chemical grafting or by physical adsorption, were reported leading to better dispersion of CNC fillers in the matrix [13,16–18]. Espino-Pérez et al. [13] showed that surface compatibilization of CNC by phenylacetic and hydrocinnamic acid helped to increase compatibility and the homogeneity of the dispersion. The well dispersed materials featured decreased the mass transport kinetics of both, O₂ and water vapor. Furthermore, grafted nanoparticles showed less swelling at high relative humidity (RH). It has been shown in polycaprolactone (PCL)/CNC nanocomposites that the diffusive pathway of water travelling along or inside the amorphous phase of the CNC percolates at high RH, where the CNC swell [19]. The grafting of CNC by phenolic acids prevented this percolation phenomenon and as a consequence the formation of a preferential diffusive pathway [13,20]. PLA/CNC nanocomposites obtained via *in-situ* ring opening polymerization [15] exhibited good filler/matrix adhesion and homogenous filler dispersion. The obtained nanocomposites provided enhancements for both water vapor and O₂ barrier properties (increase of 81% and 87%, respectively) compared to neat matrix, by using only 1 wt% of CNC. Fortunati et al. [12] showed, in contrary, no significant change or even an increase in water vapor permeability for PLA/CNC. Only a small improvement of barrier properties was obtained after using a surfactant (acid phosphate ester of ethoxylated nonylphenol) as compatibilizer. The conflicting results might be explained by the change in the morphology of PLA. CNC can have a nucleating effect on PLA. An increase in the crystallinity degree of the polymer matrix can improve the barrier properties of the system even at low CNC content. Annealing of PLA has indeed a beneficial effect on barrier properties. Sawada et al. [21] showed that the permeability coefficients of PLA to O₂ and CO₂ decreased by a factor of max. 2.6 and 2.7, respectively after annealing at 90 or 120 °C. Guinault et al. [22] and Fernandes-Nassar et al. [23] reported that at high degrees of crystallinity of PLA ($\chi_c = 50\text{--}63\%$) led to an improvement of O₂ barrier properties by a factor 4 (75%) [22] or even 6 (83%) [23]. Because of the superposition of the barrier enhancement effects of the crystallinity and the nanofiller, the specific contribution of CNC to the improvement of the properties cannot be quantified in these studies, which hinders extrapolation of results to different applicative environments. Furthermore, most existing data on O₂ permeability were obtained at 0% RH, which also imparts prediction of performance in real conditions, because it is known that the O₂ barrier properties of pure nanocellulose layers are largely dependent on the RH [24].

In the present study, we use amorphous PLA in the aim to highlight the effect of CNC on the properties of the composite. To better understand the impact of surface compatibilization, we investigated CNC bearing fatty acids or poly(glycidyl methacrylate) (PGMA) oligomers, which are able to crosslink with PLA. To show the effect of the filler volume fraction and filler percolation on the barrier properties, we aimed at preparing nanocomposites with high CNC concentration above the geometrical percolation threshold. Barrier properties to CO₂ and O₂ at different RH were measured and discussed as a function of the composite morphology and filler/matrix interfacial properties.

2. Materials and methods

2.1. Materials

Amorphous polylactide (PLA 4060D), containing $11 \pm 1\%$ D-lactic, was purchased from Resinex (France). Dichloromethane was purchased from Carlo Erba reagents (France). Spray-dried cellulose nanocrystals (CNC) were supplied by Celluforce (Canada). This nanocellulose was extracted using sulfuric acid hydrolysis from wood pulp. Surface grafted CNC with lauric acid (CNC-g-LA), stearic acid (CNC-g-SA) and poly (glycidyl methacrylate) (CNC-g-PGMA) were graciously provided in acetone suspension by the laboratory LGP2 (INP-Grenoble, Grenoble, France). The surface grafting protocol of CNC-g-LA and CNC-g-SA and detailed analysis can be found in Le Gars et al. [25] and the protocol and analysis of CNC-g-PGMA in ref. [26]. The degree of surface substitution with lauric acid (CNC-g-LA) or with stearic acid (CNC-g-SA) was 0.1 functionalized hydroxyl groups per anhydroglucose unit; the one of CNC grafted with glycidyl methacrylate (CNC-g-PGMA) was 0.2 functionalized hydroxyl groups per anhydroglucose unit. To help the reader, we repeat the detailed grafting protocols published by Le Gars et al. in the supporting information S1. The percolation threshold ($\nu = 0.7/\text{aspect ratio}$) of the different CNC was analyzed in an earlier paper. It was calculated from the observed dimensions of the CNC and amounted to approximately 9 wt% (CNC-g-LA), approximately 9 wt% (CNC-g-SA). The percolation threshold of CNC-g-PGMA was estimated equal to CNC-g-LA [18]. The percolation threshold of CNC aggregates was estimated higher than 30 wt% [18].

2.2. Production of PLA/CNC films

2.2.1. Fabrication by solvent casting

A dichloromethane (CH₂Cl₂) solution containing 10 wt% PLA was prepared by magnetic stirring overnight. The CNC suspension was prepared in CH₂Cl₂ with a concentration of 2 wt% of dry CNC. Surface modified CNC provided in acetone suspension were solvent-exchanged to CH₂Cl₂ by centrifugation followed by redispersion. The redispersed suspensions were sonicated using an ultrasound homogenization (Vibra-Cell™, USA) with an energy input of 10 kJg⁻¹. The suspensions of neat or modified CNC were added to the PLA solution. It was mixed using a homogenizer (Ultra-Turrax, IKA) for approximately 5 min and then again treated by ultrasound homogenization to ensure the dispersion of CNC within the solution and to eliminate air bubbles. The final suspension was poured into Teflon Petri dishes and left for evaporation under a laboratory hood during at least 48 h. The dried film was removed from the Petri dishes and stored in a desiccator containing silica gel, at room temperature.

2.2.2. Fabrication by extrusion

Melt-extrusion fabricated composites of PLA and CNC were prepared using a corotating twin-screw extruder Thermohaake PTW (16-40D) with a screw diameter of 16 mm and a length to diameter ratio (L/D) 40:1. The temperature profile was 160/160/160/160/170/190 °C with a screw rotation speed of 300 rpm. The materials were introduced and pre-blended using two independent dozers into the extruder's hopper. CNC were stored over silica gel in a desiccator at room temperature and PLA pellets were dried under vacuum over night at 70 °C before use. The samples prepared by twin screw extrusion contained 30 or 50 wt% CNC.

2.2.3. Compression molding of film samples

Compression molding of all samples (casted and extruded) was applied in order to homogenize the film thickness, evaporate solvent residues, release mechanical stresses, and equal thermal history and state of physical aging. The heating press from Gibitre Instruments (Italy) was used. The cast films were put in a 100 μm mold between Teflon sheets at 180 °C for 3 min without pressure and then a pressure of 150 bars was applied for 1 min. The samples were cooled down at room

temperature on the laboratory bench. The extruded strands were pelletized and the pellets were pressed using the same protocol. The thickness (L) of the individual films was measured at 10 points with an electronic caliper. In the following, the samples are named using the information of the CNC type and concentration. The CNC contents of the films are given on the basis of dry weight, i.e. 30 wt% CNC means 30 g CNC +70 g PLA. The concentration of CNC-g-PGMA was fixed with respect to CNC. Because of PGMA being a polymer surface graft, the mass of PGMA and CNC were equal. The quantity of available grafted CNC was very low (approximately 5 g of CNC-g-LA or CNC-g-SA and less than 1 g of CNC-g-PGMA). Therefore, not all concentrations could be tested using all different methodologies. A summary of the different samples and their nomenclature is provided in Table 1.

2.3. Morphological analysis

2.3.1. Gel content of PLA/CNC-g-PGMA

The PGMA surface graft bears reactive epoxy end groups [26] which can react among each other or with PLA [27] and form a covalently grafted network. The gel content of PLA/CNC-g-PGMA was determined by dissolution of 5 mg mL⁻¹ film sample in chloroform (CHCl₃) under stirring overnight. Then the CHCl₃ suspension was filtered using a pre-weighed syringe filter. The filter was dried in a vacuum oven until

Table 1
Overview of the sample set.

Name	CNC conc. (wt%)	Surface grafting method	Film fabrication	Thermo-compression
PLA			casting	yes
PLA/5 wt% CNC	5	–	casting	yes
PLA/10 wt % CNC	10	–	casting	yes
PLA/15 wt % CNC	15	–	casting	yes
PLA/20 wt % CNC	20	–	casting	yes
PLA/25 wt % CNC	25	–	casting	yes
PLA/30 wt % CNC	30	–	extrusion	yes
PLA/50 wt % CNC	50	–	extrusion	yes
PLA/5 wt% CNC-g-LA	5	surface esterification lauric acid	casting	yes
PLA/10 wt % CNC-g-LA	10	surface esterification lauric acid	casting	yes
PLA/30 wt % CNC-g-LA	30	surface esterification lauric acid	casting	yes
PLA/5 wt% CNC-g-SA	5	surface esterification stearic acid	casting	yes
PLA/10 wt % CNC-g-SA	10	surface esterification stearic acid	casting	yes
PLA/30 wt % CNC-g-SA	30	surface esterification stearic acid	casting	yes
PLA/5 wt% CNC-g-PGMA	5 wt% CNC + 5 wt% PGMA	SI-ATRP glycidyl methacrylate	casting	yes
PLA/10 wt % CNC-g-PGMA	10 wt% CNC + 10 wt% PGMA	SI-ATRP glycidyl methacrylate	casting	yes
PLA/25 wt % CNC-g-PGMA	25 wt% CNC + 25 wt% PGMA	SI-ATRP glycidyl methacrylate	casting	yes
PLA/30 wt % CNC-g-PGMA	30 wt% CNC + 30 wt% PGMA	SI-ATRP glycidyl methacrylate	casting	yes

constant weight. The gel content is expressed as the insoluble mass over initial sample mass. Each analysis was carried out twice.

2.3.2. Scanning electron microscopy (SEM)

The morphology analysis of the cross sections was done on cryo-fractured samples and on microtome cuts. An SEM EVO MA10 SEM from Zeiss was used mounted with a Tungsten electrode. The acceleration voltage was 15 kV and the work distance was 14 mm. The cross sections were sputtered with a thin layer of gold. Images acquisition was performed using the SmartSEM User Interface software.

2.3.3. Wide-Angle X-ray scattering (WAXS)

Wide-Angle X-ray Scattering experiments were carried out on the Nano-inXider SW (Xenocs) system in transmission mode using Cu K α radiation ($\lambda = 1.54 \text{ \AA}$) from an X-ray microsource (GeniX3D) operating at 50 kV-0.6 mA (30 W) (Xenocs). Scattering patterns were collected using a Pilatus3 (Dectris) detector in the aim to study the crystallinity of the CNC. 2-D data were corrected for invalid pixels, cosmic radiation, pixel dead time and detector flat-field. The corrected 2-D data were azimuthally integrated and corrected for geometrical effects (solid angle and Ewald sphere), using Foxtrot data reduction software (Version 3.4.9, Xenocs Soleil Synchrotron, France) [28], then normalized to the number of transmitted photons. After subtraction of the blank signal (spectra without sample), the WAXS profiles, $I(2\theta)$ (2θ is the Bragg angle), were analyzed to extract structural quantitative values. WAXS spectra, $I(2\theta)$, were fitted using the Fityk 0.9.8 software [29] in a wide 2θ range [5° , 60°]. With this software, the WAXS spectrum were decomposed into crystalline and amorphous contributions. The crystalline peaks are associated with sharp peaks, located at the Bragg angle $2\theta_{\text{hkl}}$, while broad peaks fit the amorphous signal. The weight crystallinity χ_c^m was calculated using the following equation:

$$\chi_c^m = \frac{A_c}{A_c + A_a} \quad (1)$$

A_c is the sum of the integrated intensities of the crystalline peaks and A_a is the total integrated intensity of the amorphous halo.

2.4. Barrier properties

2.4.1. O₂ and CO₂ permeability in dry conditions

Permeability of dry gases on films was determined with a Gas Permeability Tester (GDP-C) from Brugger (Munich, Germany) using the manometric method. The experiments were conducted at 23 °C and 0% relative humidity (RH), in accordance with ASTM D 3985. The films were purged with N₂ for 15 h under vacuum prior to the experiment. Because of the restricted availability of grafted CNC, small samples were used and adapted to the measurement device using aluminum foil. The effective surface area for measurement was 4.52 cm² and the pressure gradient was 1 atm (1.01325 bar). Data were recorded and evaluated using the CDP-C software. Permeability (P), Diffusion (D) and Solubility (S) coefficients were all determined following the time-lag method, using the equation:

$$D = \frac{L^2}{6t_{\text{lag}}}, \quad (2)$$

where t_{lag} is the induction time needed to reach the steady state of permeation. The method is described in the supporting information S2. The variation of thickness (L) and the induced error on the determination of P and D was estimated at 5% for neat PLA and 10% for PLA/CNC films. The gas permeability values are given in SI units. $P(\text{O}_2)$ is usually given in the literature in Barrer. The conversion factors are 1 Barrer = $10^{-10} \text{ cm}_3^{\text{STP}} \cdot \text{cm} \cdot \text{cm}^{-2} \cdot \text{s}^{-1} \cdot \text{cmHg}^{-1} = 7.5 \times 10^{-18} \text{ m}^3 \text{ m} \cdot \text{m}^{-2} \cdot \text{s}^{-1} \cdot \text{Pa}^{-1} = 3.35 \times 10^{-16} \text{ mol m} \cdot \text{m}^{-2} \cdot \text{s}^{-1} \cdot \text{Pa}^{-1}$.

2.4.2. O₂ permeability measurement at different RH

Oxygen permeability measurements for two hydration states (50% RH and 90% RH, respectively) were carried out using a Mocon® Oxtran (model 2/21) permeameter (Minneapolis, MN) equipped with a

coulometric sensor. The apparatus includes a test cell of two chambers divided by the tested film. The used carrier gas was nitrogen containing 2% of hydrogen (N₂/H₂) whereas the test gas was pure O₂. Aluminum masks were systematically used so that the sample's area which was

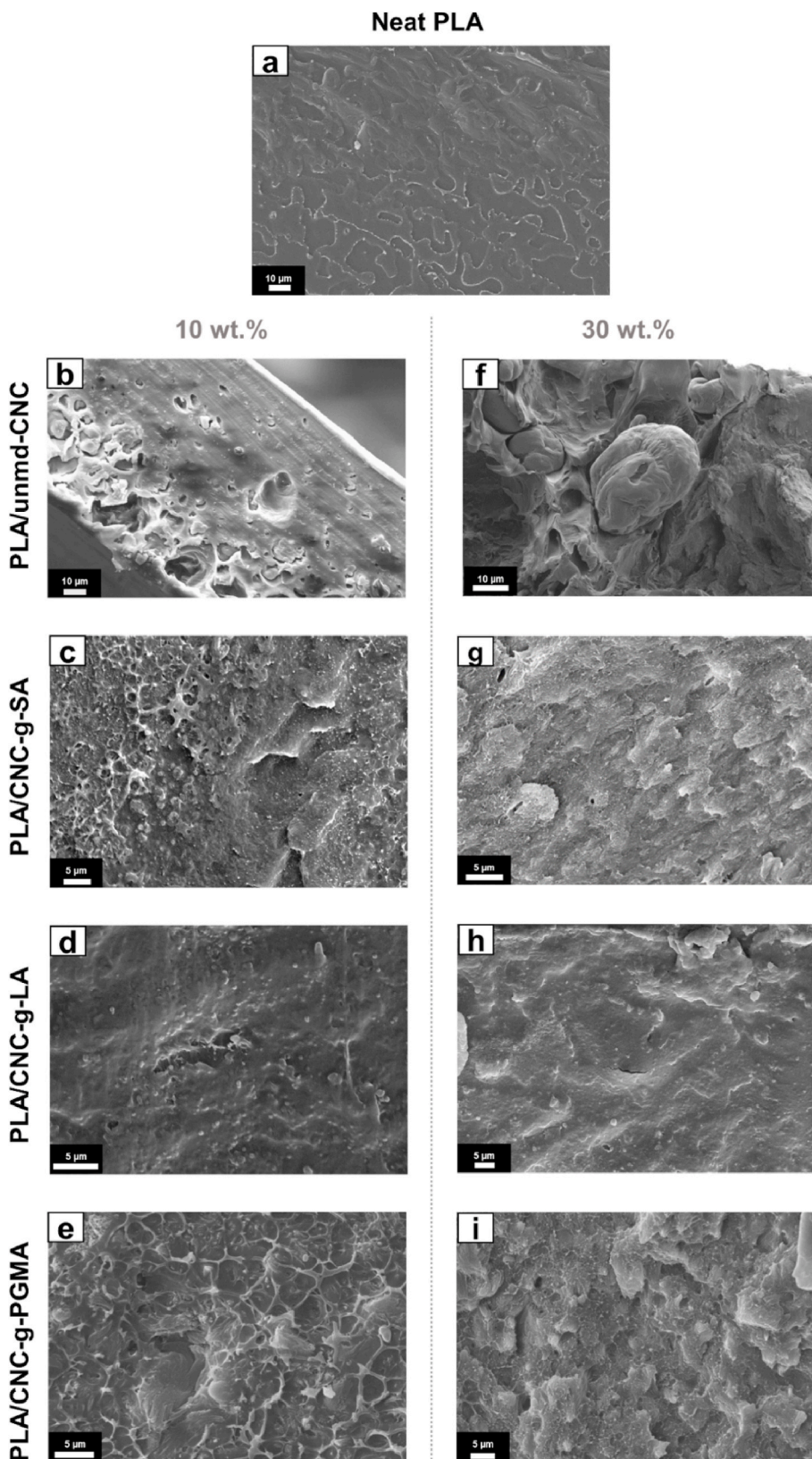


Fig. 1. SEM micrographs displaying cross sections of PLA films containing neat or surface grafted CNC: a) plain PLA, b) microtome cut cross section of cast PLA/10 wt% CNC, c) cryofracture of cast PLA/10 wt% CNC-g-SA, d) cryofracture of cast PLA/10 wt% CNC-g-LA, e) cryofracture of cast PLA/10 wt% CNC-g-PGMA, f) cryofracture of extruded PLA/30 wt% CNC, g) cryofracture of cast PLA/30 wt% CNC-g-SA, h) cryofracture of cast PLA/30 wt% CNC-g-LA, i) cryofracture of cast PLA/30 wt% CNC-g-PGMA.

exposed to the gas flow was 5 cm². The apparatus was also equipped with a humidifier to control relative humidity of both carrier and test gases. The films were preconditioned for at least 12 h in a N₂/H₂ atmosphere to achieve a “zero point”, which consist in removing all residues of O₂ or traces of nitrogen and achieving the equilibrium times of water uptake. Then, O₂ was introduced in the upstream compartment of the test cell. $P(O_2)$ was measured at a controlled temperature of 25 °C and different RH (50 and 90%). O₂ molecules transferred through the film were conducted by the carrier N₂/H₂ gas to the coulometric sensor. A steady-state line was obtained after a transitory state. The precision of the obtained values was estimated to have less than 5% error.

2.4.3. O₂ sorption measurement

The sorption isotherm measurements were performed using a gravimetric sorption apparatus IGA-001 (Hidden Analytical, UK) at 25 ± 1 °C. The samples (10–20 mg) were dried during 48 h under vacuum prior to the measurements. The mass increase was measured as a function of time for each applied pressure (from 0 to 2 bar) until reaching the equilibrium state. Then, the isothermal sorption curves corresponding to the variation of the equilibrium concentration C as a function of the pressure were plotted and fitted using the dual-mode sorption model (Equation (3)). This well-known model for gas sorption in glassy polymers combines two mechanisms: the specific sorption on specific sites C_H (Langmuir's mode) and the non-specific sorption C_D (Henry's law) [30]:

$$C = C_H + C_D = \frac{C'_H b p}{1 + b p} + k_D p, \quad (3)$$

where C'_H is the gas concentration in Langmuir sites (cavities, microvoids), p is the applied gas pressure, b the affinity constant between permeant and microvoids and k_D is Henry's coefficient representing the polymer-permeant affinity. Satisfying fit of the experimental data was defined when the average relative deviation modulus was lower than 10%.

3. Results and discussion

3.1. Morphology of the PLA/CNC nanocomposites

Fig. 1 shows the different morphologies observed from cross-sections of PLA and PLA/CNC films produced by solvent casting. Fig. 1 a exhibits the typical homogenous and regular morphology of a cryo-fractured PLA section. Fig. 1 b illustrates a typical SEM micrograph of the cross-section of a PLA film containing 10 wt% of unmodified CNC. The cross-section was inhomogeneous and showed aggregated CNCs, with sizes varying up to 30 μm. Moreover, the cross-section showed that there was sedimentation of the CNCs particles during solvent casting at the bottom of the Petri dish. PLA containing 30 wt% of CNC (Fig. 1f), which was elaborated via extrusion process, showed CNC aggregates dispersed over the whole PLA matrix (in supporting information S3 some photos and supplementary SEM images are shown). The size of single aggregate in PLA/10 wt% CNC and PLA/30 wt% CNC was between 5 and 30 μm. The surface grafted CNC-g-SA (Fig. 1c, g) and CNC-g-LA (Fig. 1d, h) were far better dispersed in the PLA matrix, even at high concentration (30 wt%). Finally, PLA films containing CNC-g-PGMA displayed in Fig. 1e and i showed also homogenous dispersion. The homogeneity of the dispersion was analyzed in our previous paper using TEM images [18], some supplementary micrographs are shown in supporting information S3. A network-like structure could be observed (light filaments in Fig. 1e, i), which was attributed to crosslinking of the PGMA grafts during the film fabrication process. PGMA bear reactive epoxy end groups, which can react among themselves or with PLA. In our earlier paper [18] the formation of phase-separated PGMA rich zones in the PLA matrix and crosslinking reactions were evidenced by DSC measurements. The gel content of PLA/CNC-g-PGMA 10 wt% before thermocompression was 22

± 5 wt%, the one of PLA/CNC-g-PGMA 30 wt% was 32 ± 5 wt% and after thermocompression 78 ± 5 wt%.

Fig. 2 shows a comparison of SEM images of PLA/25 wt% CNC obtained from cryo-fractured and PLA/50 wt% CNC microtome cut samples obtained by extrusion. There is no sedimentation of the aggregates (Fig. 2b), which confirms the SEM observation in Fig. 1. In Fig. 2a, a gap at the interface region (orange arrows) between the CNC aggregate and PLA can be observed with a length of around 500 nm. Fig. 2 b shows the cross-section of a similar aggregate. Cavities can be observed also inside the aggregate with a size up to 500 nm. Such internal voids could have a negative impact on gas barrier properties.

3.2. Crystallinity of CNC in PLA/CNC nanocomposites

Wide-Angle X-ray Scattering experiments were conducted on a selection of the obtained films in order to determine the influence of the processing technique (grafting, casting and extrusion, thermoforming) on the crystallinity of the CNCs. The raw data are provided in supporting information S4.1. The WAXS signal correspond to the superposition of two contributions: the amorphous PLA (amorphous halo at $2\theta = 16.5^\circ$) and the semi-crystalline CNC. WAXS spectra of each sample after subtraction of the PLA contribution are displayed in Fig. 3. The neat CNC fraction exhibited three main sharp peaks, at $2\theta = 14.9^\circ$, 22.5° and 34.5° (Fig. 3) in good agreement with existing data [31]. According to this publication, these three peaks (see Fig. 3a) are associated respectively with the (1–10)/(110), (200) and (004) Miller indices of the cellulose I β phase [31]. For the esterified CNC with lauric acid (Fig. 3d and e), a small shift of the second peak ($2\theta = 22.5^\circ$) compared to the neat CNC is observed. This small shift, highlighted on the zoom presented in supporting information S4.2, corresponds to a decrease of the interplanar distance d_{200} from 3.95 Å to 3.93 Å. The films with CNC-g-PGMA (Fig. 3f and g) exhibited an additional broad signal at $2\theta \sim 16^\circ$ (dotted black line in Fig. 3f and g) which might be related to the amorphous PGMA chains, it appears superimposed with the first peak of the neat CNC ($2\theta = 14.9^\circ$). Indeed, for this treatment, the amount of PGMA is significant (see Table 1), because it has the same weight fraction as the CNC.

The calculated weight crystallinity (χ_c^m) of the CNC fraction, within the composites, between 28% and 41%, was smaller than the expected crystallinity values. Indeed, to our knowledge, the only values reported in the literature are measured on CNC not incorporated in a composite. For example, the crystallinity announced by the manufacturer for pure CNC at $\chi_c = 88\%$ [32], and the values of CNC-g-LA, CNC-g-SA, and CNC-g-PGMA published by Le Gars et al. ($\chi_c \sim 83\%$) [25,26]. Even considering that the measurements were conducted using different equipment and at different conditions (the angular 2θ range is not the same), an important decrease of χ_c^m was evidenced after incorporation in composites. This result might indicate that the CNC crystals were partially destroyed due to the composite fabrication process involving high mechanical energy (ultrasounds, mechanical homogenization, extrusion) and temperature (extrusion, compression molding). To check the impact of the film fabrication process, a sample containing 10 wt% CNC was extruded for X-ray analysis (Fig. 3b). The difference in crystallinity observed in the PLA/10 wt% CNC prepared by solvent casting (Fig. 3a) and extrusion (Fig. 3b) was not significant.

3.3. Oxygen and carbon dioxide permeability measurements ($P(O_2)$ and $P(CO_2)$)

Transport properties of O₂ and CO₂ through PLA based nanocomposites were determined by permeation measurement. First, it can be seen that the $P(O_2)$ measured for neat PLA ($\sim 2.5 \cdot 10^{-18} \text{ m}^3 \text{ m}^{-2} \cdot \text{s}^{-1} \cdot \text{Pa}^{-1} = 0.33 \text{ Barrer}$) and $P(CO_2)$ ($\sim 5.6 \cdot 10^{-18} \text{ m}^3 \text{ m}^{-2} \cdot \text{s}^{-1} \cdot \text{Pa}^{-1} = 0.75 \text{ Barrer}$) were very close to those determined by Messin et al. on the same type of PLA [33], who found 0.32 Barrer and 0.75 Barrer, for O₂ and CO₂, respectively. Fig. 4a and b presents the permeability of PLA

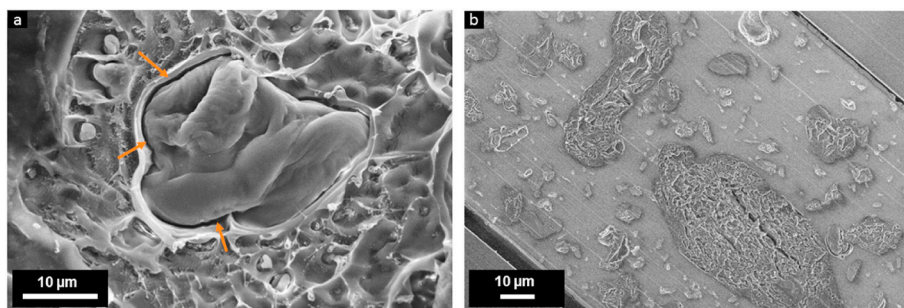


Fig. 2. SEM micrographs of CNC aggregates in extruded samples without sedimentation obtained by a) cryofracture, b) microtome. Orange arrows indicate the absence of interface and adhesion between the PLA matrix and the CNC aggregate. Scale bars represent 10 μm . (For interpretation of the references to colour in this figure legend, the reader is referred to the Web version of this article.)

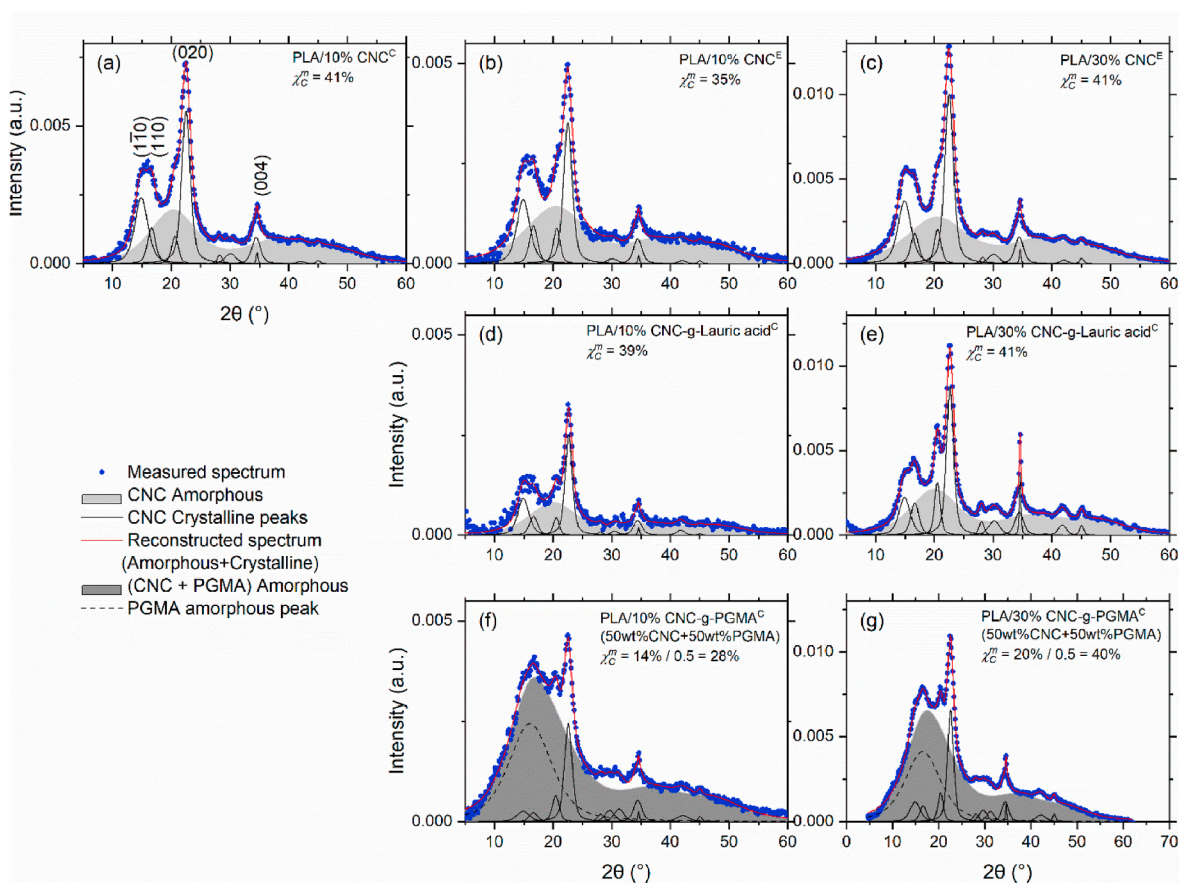


Fig. 3. WAXS diffraction patterns of PLA/CNC nanocomposites after subtraction of the amorphous halo of PLA and their calculated mass crystallinity (χ_C^m). C and E superscripts refer to the method of fabrication, C for casting and E for extrusion.

and its nanocomposites to O_2 and CO_2 , respectively. A general observation is that the addition of CNC particles enhanced the barrier properties to O_2 and CO_2 . PLA/CNC composites included large aggregates, which sedimented during the casting process. A typical result for PLA/10 wt% CNC shown in Fig. 1, supplementary results can be found in the supporting information S3. Because of the sedimentation problem, films done by solvent casting at a CNC concentration higher than 25 wt% became porous and very brittle. Therefore, the film fabrication methodology was changed to twin-screw extrusion. Surprisingly the $P(\text{O}_2)$ of PLA/30 wt% CNC, PLA/30 wt% CNC-g-LA, and PLA/30 wt% CNC-g-SA in absence of the sedimentation of the aggregates were almost equal. The decrease was approximately 40% (factor 1.6). Increase of the CNC content to 50 wt% resulted in a further decrease of $P(\text{O}_2)$, which improved by 65% (factor 2.7). Compared to literature results, the

decrease of $P(\text{O}_2)$ was similar to that can be obtained by annealing of PLA [22,23] or by the use of Montmorillonite clay [34–36]. Much less data on $P(\text{CO}_2)$ are available. The data collected by Sonchaeng et al. [34] show that the present PLA/CNC systems were competitive with PLA/nanoclay nanocomposites. The decrease in $P(\text{CO}_2)$ was similar to that of $P(\text{O}_2)$. The selectivity ($P(\text{CO}_2)/P(\text{O}_2)$) of PLA was low and tended to decrease even further in nanocomposites (Table 3). The PLA/30 wt% CNC-g-PGMA film outperformed the samples at equal CNC concentration with an enhancement factor of 2.6. This result might be attributed to crosslinking in the matrix, as attested by the gel content of 78 ± 5 wt %.

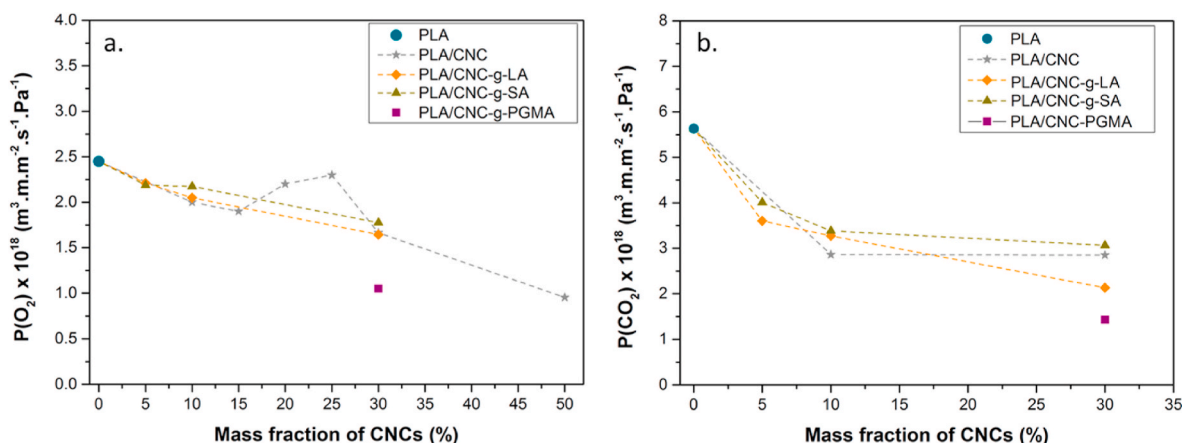


Fig. 4. Gas permeability of amorphous PLA/CNC and PLA/CNC-g-LA, PLA/CNC-g-SA and PLA/CNC-g-PGMA nanocomposites. a) Permeability of O₂ (P(O₂)) and b) Permeability of CO₂ (P(CO₂)).

3.4. Analysis of diffusion and solubility coefficients

As for gas permeability, the experimental diffusion coefficients $D(\text{O}_2)$ ($\sim 2.10 \cdot 10^{-12} \text{ m}^2 \text{ s}^{-1}$) and $D(\text{CO}_2)$ ($\sim 0.34 \cdot 10^{-12} \text{ m}^2 \text{ s}^{-1}$) determined for neat PLA agree well with literature [22,33]. To better understand these results, i.e. the relatively good performance of PLA/CNC composites despite the presence of aggregates, and the performance of PLA/CNC-g-PGMA, the evolution of the diffusion (D) and solubility (S) coefficients was investigated. Tables 2 and 3 contain the numerical data.

Different models for the prediction of the gas permeability of composites exist based on the assumption that impermeable obstacles increase the length of the tortuous pathway of permeants, which decreases D . The simplified Maxwell model for predicting the diffusivity in the composite system assumes impermeable dispersed spheres. It can be expressed as [37]:

$$\frac{D_c}{D_m} = \frac{1}{1 + \left(\frac{v_r}{2}\right)}, \quad (4)$$

where D_c and D_m are respectively the diffusion coefficient of the composite and the matrix (here PLA), and v_r the theoretical volume fraction of CNCs in the matrix.

Nielsen's model takes into consideration the aspect ratio of the square or circular platelets of infinite lengths dispersed uniformly in the matrix. It is written as follows [37,38]:

$$\frac{D_c}{D_m} = \frac{1}{1 + \left(\frac{L}{2W}\right)v_r}, \quad (5)$$

where L and W are the length and diameter of the CNC, respectively (aspect ratio = L/W). Bharadwaj proposed an extension which takes into account the orientation of the fillers by introducing a factor of orientation order S . In the case of random orientation, $S = 0$. The resulting equation is written as [37,39]:

$$\frac{D_c}{D_m} = \frac{1}{1 + \left(\frac{L}{2W}\right)v_r \left(\frac{2}{3}\right) \left(S + \frac{1}{2}\right)}, \quad (6)$$

We measured the size of CNC, CNC-g-LA and CNC-g-SA by transmission electron microscopy (TEM) and reported on it in an earlier paper [18]. The analysis was done on isolated particles, because the low contrast of the TEM and SEM pictures prevented the determination of the aspect ratio in the PLA matrix. Additional SEM and TEM images of the film morphology are shown in the supporting information S3. The aspect ratios were: L/W (CNC) = 23.3, L/W (CNC-g-LA) = 10.7, L/W (CNC-g-SA) = 11.3. Fig. 1 shows that CNC were aggregated in the PLA matrix. Therefore, we assumed an elliptical form for CNC in the PLA/CNC composites with L/W (CNC aggregates) = 2. The modeling of

the evolution of the relative oxygen and carbon dioxide diffusion coefficients of the composites with increasing filler volume fraction in the samples and taking into account the measured aspect ratio are displayed in Fig. 5. The results obtained using of both gas types are therefore displayed in the same figure. Fig. 5 a shows a very small decrease in the relative D with increasing neat CNC volume fraction. Below 20 wt% of CNC, D_c/D_m was higher than unity, which means that the permeability of composite was higher than the permeability of the neat matrix. This result is linked to the morphology of the films which contain sedimented aggregates and a lack of interfacial cohesion between matrix and filler. In absence of sedimentation (films obtained by extrusion containing 30 or 50 wt% CNC), a small decrease in D_c/D_m was observed. We identified that the Nielsen model described not very satisfyingly the properties of the samples without sedimentation using the determined form factor of 2. A higher L/W ratio would be needed for better description, but such a change cannot be inferred from the morphology study.

Fig. 5b and c shows the evolution of D_c/D_m in nanocomposites with compatibilized interfaces and without large-size aggregates. At volume fractions of CNC <10 vol%, almost no decrease in diffusivity was observed. The Nielsen model considers a geometrical tortuosity factor to describe the decrease of D with increasing volume fraction of impermeable fillers in the matrix. Its fit of $D(\text{CO}_2)$ and $D(\text{O}_2)$ at high volume fraction of CNC-g-LA was correct (Fig. 5c), while the Nielsen model underestimated the D_c/D_m in PLA/CNC-g-SA (Fig. 5b). The surface grafting of CNC increased the compatibility between phases and the homogeneity of the dispersion (Fig. 1). We showed in our previous work using differential scanning calorimetry and dynamic mechanical analysis, that the interaction at the interface of CNC-g-LA or CNC-g-SA with PLA was globally weak [18]. Comparing the effects of both types of surface grafts, we showed that the PLA/CNC-g-LA interfaces were more cohesive than the PLA/CNC-g-SA interfaces. This difference might be the reason of the higher D_c/D_m in PLA/CNC-g-SA nanocomposites. In conclusion, the impact of surface-compatibilized CNC on the diffusivity of O₂ and CO₂ can be described by the Nielsen model. The evolution is consistent with the tortuosity obtained with impermeable and non-oriented fillers.

The PLA/30 wt% CNC-g-PGMA showed equal D_c/D_m . The morphology of these samples was characterized by a phase-separated PGMA fraction, forming a network like structure, probably partially crosslinked with PLA and containing well-dispersed CNC crosslinked with each other (Fig. 1). Previous studies [40] underlined the beneficial impact of network-like structure composed of fillers on barrier properties. In the present case, the crosslinking taking place in the interfacial area might bring an additional contribution in the reinforcement of the barrier properties, explaining the higher barrier performance obtained with PLA/CNC-g-PGMA although the tortuosity factor expressed by

Table 2

Oxygen permeation parameters of PLA and its nanocomposites. The error in the measurements is due to the variability in the thicknesses of the films (5–10 wt %).

Sample	Thickness (μm)	$D(O_2)$ (10^{-12} m ² /s)	$P(O_2)$ (10^{-18} m ³ m/m ² .s. Pa)	$S(O_2)$ (10^{-6} m ³ /m ³ . Pa)	Normalized $S_n(O_2)$ (10^{-6} m ³ /m ³ . Pa)
PLA	128	1.93	2.47	1.28	1.28
PLA	105	1.98	2.59	1.31	1.31
PLA	142	2.10	2.54	1.21	1.21
PLA/10 wt % CNC	95	2.16	1.39	0.64	0.70
PLA/15 wt % CNC	130	4.32	2.56	0.59	0.67
PLA/20 wt % CNC	110	2.87	2.24	0.78	0.94
PLA/25 wt % CNC	99	2.51	2.31	0.92	1.17
PLA/30 wt % CNC	154	1.26	1.37	1.09	1.47
PLA/50 wt % CNC	165	0.86	0.92	1.07	1.94
PLA/5 wt% CNC-g-LA	188	2.15	2.21	1.03	1.07
PLA/5 wt% CNC-g-LA	188	2.21	2.20	1.00	1.04
PLA/10 wt % CNC-g-LA	239	2.04	2.20	1.08	1.18
PLA/10 wt % CNC-g-LA	239	2.50	1.90	0.76	0.83
PLA/30 wt % CNC-g-LA	88	0.94	1.64	1.75	2.36
PLA/5 wt% CNC-g-SA	94	2.49	2.19	0.88	0.92
PLA/10 wt % CNC-g-SA	134	1.74	2.18	1.25	1.36
PLA/30 wt % CNC-g-SA	113	1.72	1.81	1.05	1.42
PLA/30 wt % CNC-g-SA	113	1.63	1.74	1.07	1.44
PLA/30 wt % CNC-g-PGMA	159	1.01	1.05	1.04	1.40

*normalized values computed assuming the density of PLA equal to 1.24 and the density of CNC equal to 1.52 attributing the gas sorption only to the PLA phase.

D_c/D_m was not very different from the other systems.

In addition to the diffusion coefficient, the gas solubility coefficient S is also a key parameter for barrier properties. The sample preparation method reduced the crystallinity degree of the CNC from initially 88% (supplier information) to approximately 40% (Fig. 3). Solubility of O_2 and CO_2 can therefore be expected not only in PLA, but also at the interface, in the internal cavities of agglomerates (observed in Figs. 1 and 2), and to a small amount, taking into account the polarity of cellulose, inside the CNC. Table 2 shows the evolution of the solubility coefficient (S) with increasing weight fraction of CNC. In the aim to ease interpretation, a normalized S_n was calculated, which corresponds to the gas sorption within the amorphous PLA. For this calculation, it was assumed that the volume occupied by CNC is excluded volume and does not sorb O_2 or CO_2 . An increase of S_n to a value higher than that of PLA will thus indicate the generation of supplementary free volume in the structure able to take up gas molecules. Because of the experimental uncertainty of the data, it can be only concluded on tendencies, though.

Table 3

Carbon dioxide permeation parameters of PLA and its nanocomposites. The error in the measurements is due to the variability in the thicknesses of the films (5–10 wt %).

Samples	Thickness (μm)	$D(CO_2)$ (10^{-13} m ² /s)	$P(CO_2)$ (10^{-18} m ³ m/m ² .s. Pa)	S (CO_2) (10^{-5} m ³ /m ³ . Pa)	Normalized $S_n(CO_2)$ (10^{-5} m ³ /m ³ .Pa)	P (CO_2)/ $P(O_2)$
PLA	96	3.64	5.50	1.51	1.51	2.22
PLA	128	3.10	5.15	1.66	1.66	1.99
PLA	96	3.45	6.24	1.81	1.81	2.46
PLA/10 wt% CNC	192	2.60	2.86	1.10	1.20	2.06
PLA/30 wt% CNC	205	3.87	2.85	0.74	1.00	2.08
PLA/5 wt% CNC-g-LA	188	2.98	3.40	1.14	1.19	1.53
PLA/5 wt% CNC-g-LA	188	3.84	3.80	0.99	1.08	1.73
PLA/10 wt% CNC-g-LA	239	3.11	3.30	1.06	1.16	1.50
PLA/10 wt% CNC-g-LA	239	3.17	3.23	1.02	1.38	1.70
PLA/30 wt% CNC-g-LA	88	1.44	2.13	1.48	1.54	1.30
PLA/5 wt% CNC-g-SA	94	2.28	3.88	1.70	1.77	1.77
PLA/5 wt% CNC-g-SA	94	2.22	4.15	1.87	2.04	1.89
PLA/10 wt% CNC-g-SA	134	2.92	3.42	1.17	1.28	1.57
PLA/10 wt% CNC-g-SA	134	2.79	3.35	1.20	1.31	1.54
PLA/30 wt% CNC-g-SA	113	2.13	3.07	1.44	1.94	1.76
PLA/30 wt% CNC-g-PGMA	159	1.90	1.43	0.75	1.01	1.36

According to the used methodology, no overconcentration of $S(CO_2)$ could be observed (Table 3), showing that no supplementary sorption sites are created in nanocomposites with respect to neat PLA matrix. In the case of O_2 a small increase in solubility with increasing concentration of CNC was obtained when the quantity of CNC was high (30 or 50 wt%), but no difference could be observed as a function of the CNC surface properties.

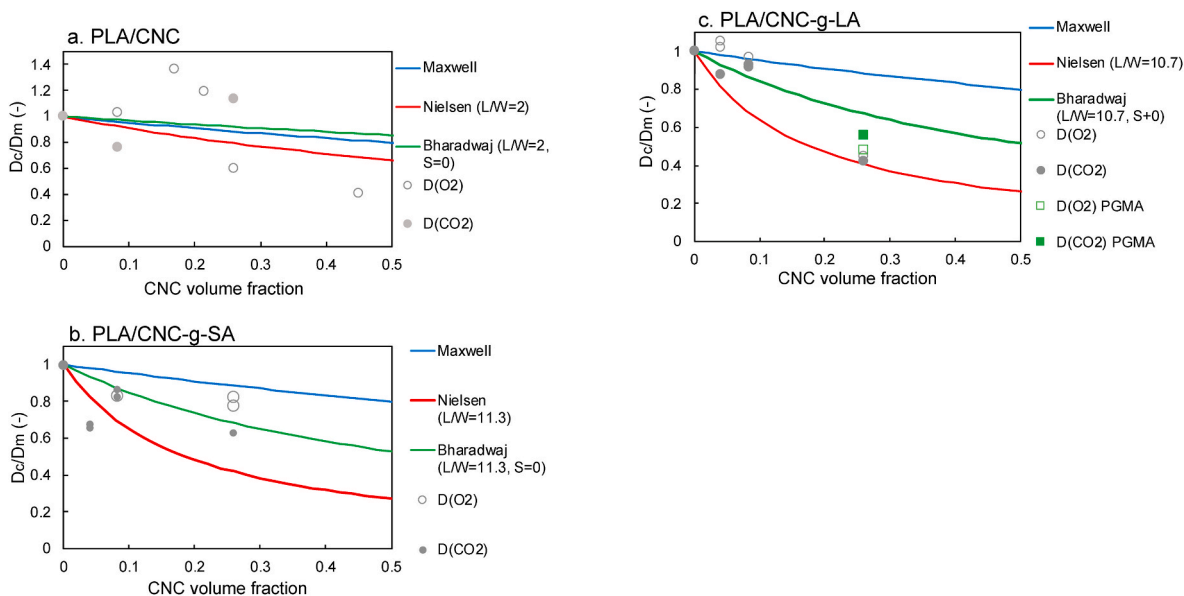


Fig. 5. Evolution of relative diffusion coefficient of PLA/CNC composites as a function of CNC volume fraction. Comparison between the experimental data and predictive models.

3.5. Oxygen solubility in PLA/CNC nanocomposites

The determination of the solubility coefficient from the permeability and diffusion coefficient is an indirect measurement which is thus subject to high uncertainty, therefore we carried out a direct measurement. In this part, only O_2 was tested on the blank samples and the most promising nanocomposites (PLA-g-LA and PLA-g-PGMA). Fig. 6 shows the O_2 sorption isotherm curves of PLA and its nanocomposites, which were fitted with the dual-sorption mode (Equation (3)), commonly admitted to be valid for glassy polymers [41]. The dual mode sorption model supposes that two types of sorption sites exist inside the glassy polymer, *i.e.* sites obeying Henry's law of dissolution in the polymer and sites obeying Langmuir's isotherm in porous solids. The "porous" character would arise from the existence of excess free volume (microvoids)

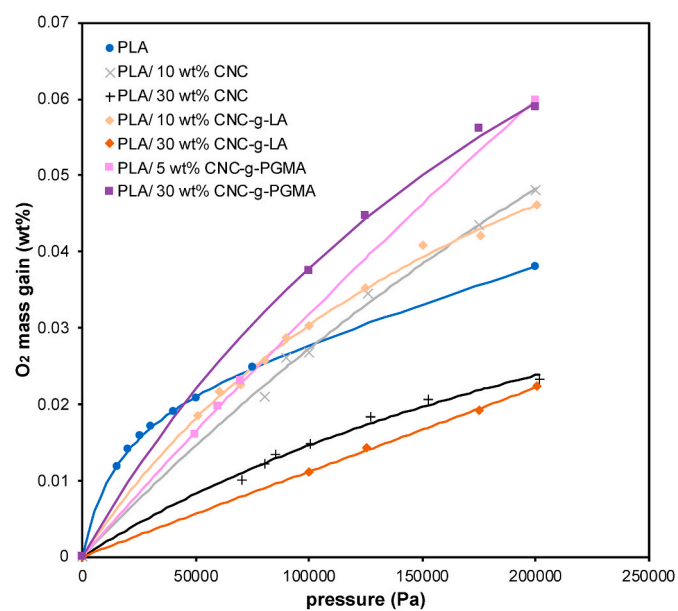


Fig. 6. O_2 sorption isotherms of PLA, PLA/CNC, PLA/CNC-g-LA, and PLA/CNC-g-PGMA nanocomposites. The symbols show the experimental data and the lines the dual-sorption model (equation (3)).

due to the non-equilibrium state of polymer glasses (Equation (3)). PLA shows Langmuir-type sorption, a behavior which was predicted by molecular modelling [42]. The calculated model parameters are given in Table 4. The O_2 solubility at 1 atm was calculated and compared to the obtained values from the permeability experiment. The data obtained from the direct measurement of O_2 sorption (Table 4) were found higher but in the same order of magnitude than the values inferred from the permeability experiment (Table 2), which agrees with $P = DS$ assuming D constant. The fact that $S(O_2)$ determined in sorption is higher as high as that deduced in permeation is probably due to the fact that the initial conditions and measurement set-up and boundary conditions in permeation and in sorption are not the same.

Fig. 6 shows that the O_2 sorption isotherms of nanocomposites containing CNC-g-PGMA crossed the sorption isotherm of PLA before 1 atm. The weight ratio of CNC and PGMA was 1:1, which means that the sample containing 25 wt% would be composed of 50 wt% PLA + 25 wt% CNC + 25 wt% PGMA. This might explain the substantial change in the sorption isotherm. The sorption isotherms of the nanocomposites containing 10 wt% of filler crossed also the isotherm of PLA at around 1 atm. The observation of the ranking of the curves at this pressure is coherent with the estimation done using the permeability experiments. The presence of less than 10 vol% CNC did not reduce the sorption capacity of the material. Apparently, supplementary sorption sites were created, cancelling out the excluded volume effect of a polar and crystalline filler. Interestingly, the surface grafting of the CNC did not change the behavior. Cavities which might be opened by low interface bonding did not seem to dominate the sorption behavior. The same result was obtained with nanocomposites containing 30 wt% of nanofiller, although here the sorption capacity seemed to be lowered with regards to PLA. This was not coherent with the estimation from the permeability experiment. We think that the sorption isotherm might be underestimated because of the small experimental times, which maybe did not allow to reach the sorption equilibrium for the samples with the lowest diffusion coefficients. To tend to correlate sorption results to those of permeation, it was then interesting to estimate the oxygen permeability at 1 bar from sorption experiment.

From the dual-mode sorption model and assuming a Fickian behavior, it is possible to predict the variation of the oxygen permeability as function of the oxygen pressure. Indeed as shown by Stern et al. [43] the permeability coefficient can be expressed using the parameters of the dual sorption law as:

Table 4

Quantification of the O₂ sorption isotherms in PLA and its nanocomposites. The parameters C_H, b and K_D were calculated using from the dual-sorption model (equation (3) and (7)) and S the sorption coefficient was measured at ~1 bar.

	Mass gain (wt %)	C _H (cm ³ .cm ⁻³)	b (10 ⁻⁵ Pa ⁻¹)	k _D (10 ⁻⁸ cm ³ cm ⁻³ Pa ⁻¹)	S(O ₂) (10 ⁻⁶ m ³ m ⁻³ Pa ⁻¹)	D _D (10 ⁻¹¹ m ² /s)	D _H (10 ⁻¹¹ m ² /s ⁻¹)	P (10 ⁻¹⁸ m ³ m ² .s Pa)
Neat PLA	0.028	0.02191	6.09	8.87	3.0	2.10	2.10	5.8
PLA/10 wt% CNC	0.027	0.20710	0.150	0.203	2.9	0.80	1.17	3.2
PLA/30 wt% CNC	0.015	0.06299	0.299	0.0098	1.6	1.12	2.57	3.7
PLA/10 wt% CNC-g-LA	0.030	0.08849	0.497	0.983	3.3	4.47	3.64	10.9
PLA/30 wt% CNC-g-LA	0.011	0.00071	0.707	10.9	1.2	1.18	2.09	1.35
PLA/5 wt% CNC-g-PGMA	0.032	0.50560	0.0668	0.150	3.5	1.34	3.17	10.0
PLA/30 wt% CNC-g-PGMA	0.038	0.13630	0.383	0.248	4.1	0.62	3.02	11.2

$$P = k_D \cdot D_D \left[1 + \frac{K \cdot F}{(1 + bP)} \right] \quad (7)$$

where $F = D_H/D_D$ (D_H and D_D , the diffusion coefficients corresponding to the Langmuir and Henry parts) and $K = C_H b/k_D$

By using the fitted parameters of the dual-mode model applied to the oxygen sorption isotherm curves (Table 4), the $P(O_2)$ values were calculated (equation (7)) as function of oxygen pressure. For comparison, the predicted oxygen permeabilities estimated at 1 bar (Table 4) of PLA and PLA/CNC composites and the PLA/30 wt% CNC-g-LA are in the same order of magnitude than those obtained from permeation experiments (Table 2). For the other samples, the calculated values of oxygen permeability deduced from sorption experiments are roughly ten times higher than those determined in permeation. Direct sorption measurements are difficult to be carried out because the sorbed mass is very small and close to the detection limit of the microbalance. Therefore, these measurements have uncertainty, only the samples containing 30 wt% of CNC and CNC-g-LA can be considered different from the PLA at the point of the isotherm at 1 bar. Again, as previously explained for solubility, in sorption and permeation experiments, not only the boundary conditions are not the same but neither are the gradient of oxygen pressures, nor the time scale of process. Therefore, it can be expected that the diffusion coefficients measured in sorption and permeation are different. Despite this discrepancy, both sorption and permeation results show an improvement of oxygen barrier effect for PLA/10 wt% CNC, PLA/30 wt% CNC and PLA/30 wt% CNC-g-LA in comparison with neat PLA. It seems that the origin of this barrier effect is due to both the decrease of oxygen diffusivity and solubility but in a different way according to the experimental conditions of the oxygen penetration. Indeed, as shown from sorption isotherms, it can be seen that the oxygen sorption capacities of loaded PLA films can be higher or lower than that of neat PLA depending on the applied oxygen pressure range. However, for PLA loaded with 30 wt% of CNC or CNC-g-LA, their sorption capacity remains lower whatever the pressure. From that, it would have been interesting to see how the oxygen permeability varies with oxygen pressure, knowing that in the case of a dual-mode sorption it is expected that the gas permeability decreases with the increase gas pressure until reaching a constant minimum value once the Langmuir sorption sites are saturated.

3.6. Oxygen permeability of PLA/CNC nanocomposites at different relative humidity

Oxygen barrier properties of cellulose-based nanomaterials, in particular CNCs, are known to be negatively affected by the relative humidity of the environment. Numerous studies showed this behavior though published data [44]. Martínez-Sanz et al. [45] presented interesting results on bacterial CNC films, which revealed that the permeability to oxygen of CNC increased drastically, by a factor of over 8500

when the RH increased from 0 to 80%. Previous works showed the same trend in microfibrillated cellulosic films and coatings [46]. This phenomenon is typical of hydrophilic materials, due to the plasticization effects of water on cellulose. Indeed, the hydroxyl groups responsible for maintaining the dense, high barrier CNC network are disrupted in the presence of water molecules, causing a weakening in the structure of the films, thus allowing oxygen molecules to rapidly penetrate the films due to the newly generated free volume.

Fig. 7 shows the evolution of O₂ permeability in PLA and its nanocomposites. Firstly, it is important to note that $P(O_2)$ measurements of PLA and its nanocomposites were performed using a different measurement methodology depending on the RH value, i.e. manometric detection at 0% RH and coulometric detection at 50 and 80% RH. Taking into account the uncertainty due to the different methods, the $P(O_2)$ of PLA decreased as the relative humidity increased from 0 to 50 wt% RH, then it remained constant. A similar behavior was already observed by Kuanusont et al. [47] on blown PLA films. Other reports showed that $P(O_2)$ of PLA remained almost constant when the relative humidity was increased (from 0 to 75%) [48,49]. Tenn et al. [49] observed a slight decrease of $P(O_2)$ which varied from $1.9 \cdot 10^{-18} \text{ m}^3 \text{ m}^{-2} \cdot \text{s}^{-1} \cdot \text{Pa}^{-1}$ (0% RH) to $1.5 \cdot 10^{-18} \text{ m}^3 \text{ m}^{-2} \cdot \text{s}^{-1} \cdot \text{Pa}^{-1}$ (at 50% RH). However, they observed then an increase to $2.2 \cdot 10^{-18} \text{ m}^3 \text{ m}^{-2} \cdot \text{s}^{-1} \cdot \text{Pa}^{-1}$ at 90% RH. All these data are in the range of oxygen permeability found in this work for PLA. The nanocomposites had enhanced barrier properties with respect to the neat PLA matrix. The better O₂ barrier was maintained at

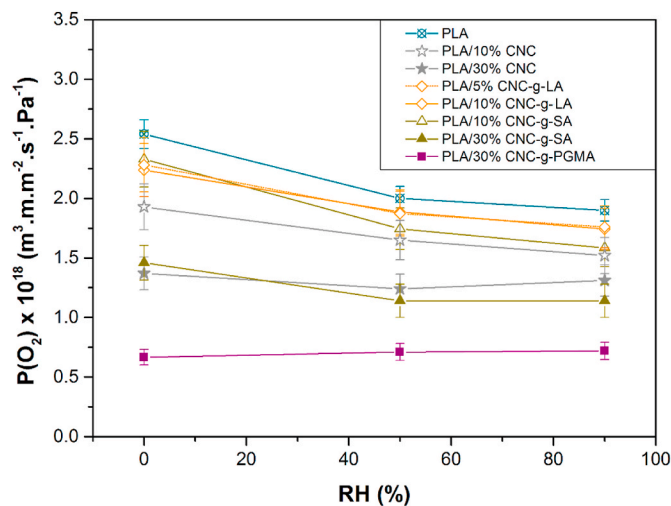


Fig. 7. Effect of relative humidity (RH) on the O₂ permeability ($P(O_2)$) of PLA, PLA/CNC, PLA/CNC-g-LA, PLA/CNC-g-SA and PLA/CNC-g-PGMA nanocomposites with different concentrations. Error bars represent the error induced by the imprecision in the thickness measurements.

high RH. The PLA matrix granted the necessary protection of CNC from humidity and swelling. This avoided the $P(O_2)$ increase observed in CNC layers at high RH [50]. The grafting of the CNC surface seemed to improve further the shielding of CNC at high RH. To summarize, the variation of relative humidity did not alter the oxygen permeability coefficients. This result highlights the relevance of the particular system of nanocomposite in comparison to its coating counterpart. The PLA behaved as a protective layer to the CNC from humidity, CNC were embedded into the PLA matrix which allowed them to maintain their contribution to the enhancement of barrier properties to oxygen, through the effect of tortuosity. As a consequence, best performance was observed at 30 wt% nanofiller and the lowest $P(O_2)$ was obtained with PLA/30 wt% CNC-g-PGMA. It remained constant in the whole range of RH values.

4. Conclusion

The mass transport parameters of gas permeability through amorphous PLA/CNC nanocomposites were analyzed with the aim to understand the impact of interface properties and aggregates on the overall performance. For that, nanocomposites prepared from CNC bearing non-interacting (stearic acid), interacting (lauric acid) and crosslinking (PGMA) molecules were prepared. Each type of nanocomposite was investigated over a large nanofiller concentration interval (5–50 wt%). The evolution of the diffusion coefficients of O_2 or CO_2 measured in dry state could be successfully modeled with Nielsen's model, showing that the geometrical factor of tortuosity largely dominates the behavior and outweighs interface effects. The higher barrier performance of compatibilized CNC with regards to neat CNC can be explained by the difference of their effective aspect ratio in the nanocomposite. Crosslinking caused a supplementary gain in performance. The indirect analysis of the nanocomposite gas sorption inferred from the permeability experiments showed that the presence of the nanofillers did induce some overconcentration of O_2 in the materials due to sorption in CNC voids or interfaces. The direct analysis of O_2 sorption using a microbalance showed that supplementary sorption sites can be generated by CNC in the nanocomposites no matter the type of surface grafting. The neglectable evolution of the O_2 barrier properties with increasing RH showed that, the barrier properties of the nanocomposites in relevant applicative environments at high RH (90%) can be maintained. Although the gains in oxygen barrier property of nanocomposites were lower than that of CNC multilayer materials, their properties were more stable in service conditions. Surface grafting of CNC increased performance, where the use of lauric acid seemed to be an optimal choice, combining barrier performance, non-toxicity and a simple grafting protocol.

Note on funding

The project was funded by the National French Research agency - ANR-16-CE08-0040 - GASP.

Credit author statement

Hajar Faraj: Conceptualization, Investigation, Methodology, Writing - Original Draft. Nadège Follain: Investigation, Methodology, Writing - Original Draft. Cyrille Sollogoub: Conceptualization, Investigation, Writing - Original Draft. Giana Almeida: Investigation, Methodology. Corinne Chappey: Investigation, Methodology. Stéphane Marais: Investigation, Methodology, Writing - Original Draft. Sylvie Tencé-Girault: Conceptualization, Investigation, Methodology, Writing - Original Draft, Review & Editing. Fabrice Gouanvé: Investigation, Methodology, Writing - Original Draft. Eliane Espuche: Investigation, Methodology, Writing - Original Draft. Sandra Domenek: Conceptualization, Investigation, Project administration, Writing - Original Draft, Review & Editing.

Declaration of competing interest

The authors declare that they have no known competing financial interests or personal relationships that could have appeared to influence the work reported in this paper.

Acknowledgements

Funding: This work was supported by the National French Research Agency (ANR), project ANR-16-CE08-0040-01 GASP.

The authors acknowledge the help of Anir Benihya (IE INRAE) member of the UMR SayFood (AgroParisTech/INRAE/Université Paris-Saclay) in the analysis of the gel content.

Sylvie Tencé-Girault's contribution was achieved within the framework of the Industrial Chair Arkema (Arkema/CNRS-ENSAM-Cnam, Arkema N° AC-2018-413, CNRS N° 183697).

Appendix A. Supplementary data

Supplementary data to this article can be found online at <https://doi.org/10.1016/j.polymeresting.2022.107683>.

References

- [1] J.-M. Lagarón, Poly(lactic Acid) (PLA) Nanocomposites for Food Packaging Applications, Multifunctional and Nanoreinforced Polymers for Food Packaging, 2011, pp. 485–497. Elsevier.
- [2] E. Vatanever, D. Arslan, M. Nofar, Poly(lactide cellulose)-based nanocomposites, *Int. J. Biol. Macromol.* 137 (2019) 912–938, <https://doi.org/10.1016/j.ijbiomac.2019.06.205>.
- [3] H.-Y. Yu, H. Zhang, M.-L. Song, Y. Zhou, J. Yao, Q.-Q. Ni, From cellulose nanospheres, nanorods to nanofibers: various aspect ratio induced nucleation/reinforcing effects on poly(lactic acid) for robust-barrier food packaging, *ACS Appl. Mater. Interfaces* 9 (2017) 43920–43938.
- [4] T.P. Haider, C. Volker, J. Kramm, K. Landfester, F.R. Wurm, Plastics of the future? The impact of biodegradable polymers on the environment and on society, *Angew. Chem., Int. Ed.* 58 (2019) 50–62, <https://doi.org/10.1002/anie.201805766>.
- [5] E. Mascheroni, R. Rampazzo, M.A. Orteni, G. Piva, S. Bonetti, L. Piergiovanni, Comparison of cellulose nanocrystals obtained by sulfuric acid hydrolysis and ammonium persulfate, to be used as coating on flexible food-packaging materials, *Cellulose* 23 (2016) 779–793, <https://doi.org/10.1007/s10570-015-0853-2>.
- [6] A. Ferrer, L. Pal, M. Hubbe, Nanocellulose in packaging: advances in barrier layer technologies, *Ind. Crop. Prod.* 95 (2017) 574–582, <https://doi.org/10.1016/j.indcrop.2016.11.012>.
- [7] R.A. Chowdhury, M. Nuruddin, C. Clarkson, F. Montes, J. Howarter, J. P. Youngblood, Cellulose nanocrystal (CNC) coatings with controlled anisotropy as high-performance gas barrier films, *ACS Appl. Mater. Interfaces* 11 (2019) 1376–1383.
- [8] N.S. Sangaj, V.C. Malshe, Permeability of polymers in protective organic coatings, *Prog. Org. Coating* 50 (2004) 28–39.
- [9] H. Kargarzadeh, M. Mariano, J. Huang, N. Lin, I. Ahmad, A. Dufresne, S. Thomas, Recent developments on nanocellulose reinforced polymer nanocomposites: a review, *Polymer* 132 (2017) 368–393.
- [10] T. Htira, S. Zid, M. Zinet, E. Espuche, Finite element analysis of gas diffusion in polymer nanocomposite systems containing rod-like nanofillers, *Polymers* 13 (2021) 2615.
- [11] M. Sanchez-Garcia, J. Lagaron, On the use of plant cellulose nanowhiskers to enhance the barrier properties of poly(lactic acid), *Cellulose* 17 (2010) 987–1004.
- [12] E. Fortunati, M. Peltzer, I. Armentano, L. Torre, A. Jiménez, J. Kenny, Effects of modified cellulose nanocrystals on the barrier and migration properties of PLA nano-biocomposites, *Carbohydr. Polym.* 90 (2012) 948–956.
- [13] E. Espino-Pérez, J. Bras, G. Almeida, C. Plessis, N. Belgacem, P. Perré, S. Domenek, Designed cellulose nanocrystal surface properties for improving barrier properties in poly(lactide) nanocomposites, *Carbohydr. Polym.* 183 (2018) 267–277.
- [14] M. Martínez-Sanz, M.A. Abdelwahab, A. Lopez-Rubio, J.M. Lagaron, E. Chiellini, T. G. Williams, D.F. Wood, W.J. Orts, S.H. Imam, Incorporation of poly(glycidylmethacrylate) grafted bacterial cellulose nanowhiskers in poly(lactic acid) nanocomposites: improved barrier and mechanical properties, *Eur. Polym. J.* 49 (2013) 2062–2072.
- [15] C. Miao, W.Y. Hamad, In-situ polymerized cellulose nanocrystals (CNC)—poly(l-lactide) (PLLA) nanomaterials and applications in nanocomposite processing, *Carbohydr. Polym.* 153 (2016) 549–558.
- [16] S.A. Kedzior, J.O. Zoppe, R.M. Berry, E.D. Cranston, Recent advances and an industrial perspective of cellulose nanocrystal functionalization through polymer grafting, *Curr. Opin. Solid State Mater. Sci.* 23 (2019) 74–91.
- [17] A. Chakrabarty, Y. Teramoto, Recent advances in nanocellulose composites with polymers: a guide for choosing partners and how to incorporate them, *Polymers* 10 (2018) 47.

- [18] H. Faraj, C. Sollogoub, A. Guinault, M. Gervais, J. Bras, H. Salmi-Mani, P. Roger, M. Le Gars, S. Domenek, A comparative study of the thermo-mechanical properties of polylactide/cellulose nanocrystal nanocomposites obtained by two surface compatibilization strategies, *Mater. Today Commun.* 29 (2021), 102907.
- [19] N. Follain, S. Belbekhouche, J. Bras, G. Siqueira, S. Marais, A. Dufresne, Water transport properties of bio-nanocomposites reinforced by *Luffa cylindrica* cellulose nanocrystals, *J. Membr. Sci.* 427 (2013) 218–229.
- [20] G. Almeida, S. Domenek, P. Perré, TransPoly: a theoretical model to quantify the dynamics of water transfer through nanostructured polymer films, *Polymer* 191 (2020), 122256.
- [21] H. Sawada, Y. Takahashi, S. Miyata, S. Kanehashi, S. Sato, K. Nagai, Gas transport properties and crystalline structure of poly(lactic acid) membranes, *Trans. Mater. Res. Soc. Japan* 35 (2010) 241–246.
- [22] A. Guinault, C. Sollogoub, V. Ducruet, S. Domenek, Impact of crystallinity of poly(lactide) on helium and oxygen barrier properties, *Eur. Polym. J.* 48 (2012) 779–788.
- [23] S. Fernandes Nassar, A. Guinault, N. Delpouve, V. Divry, V. Ducruet, C. Sollogoub, S. Domenek, Multi-scale analysis of the impact of polylactide morphology on gas barrier properties, *Polymer* 108 (2017) 163–172.
- [24] H. Fukuzumi, T. Saito, A. Isogai, Influence of TEMPO-oxidized cellulose nanofibril length on film properties, *Carbohydr. Polym.* 93 (2013) 172–177.
- [25] M. Le Gars, P. Roger, N. Belgacem, J. Bras, Role of solvent exchange in dispersion of cellulose nanocrystals and their esterification using fatty acids as solvents, *Cellulose* 27 (2020) 4319–4336.
- [26] M. Le Gars, J. Bras, H. Salmi-Mani, M. Ji, D. Dragoe, H. Faraj, S. Domenek, N. Belgacem, P. Roger, Polymerization of glycidyl methacrylate from the surface of cellulose nanocrystals for the elaboration of PLA-based nanocomposites, *Carbohydr. Polym.* 234 (2020), 115899.
- [27] H. Faraj, C. Sollogoub, A. Guinault, M. Gervais, J. Bras, H. Salmi-Mani, P. Roger, M. Le Gars, S. Domenek, A Comparative Study of the Thermo-Mechanical Properties of Polylactide/cellulose Nanocrystal Nanocomposites Obtained by Two Surface Compatibilization Strategies, *Macromolecular Materials and Engineering*, 2021 under revision.
- [28] As of April 19, the software can be obtained by sending a mail to foxtrot@xenocs.com. Software is free for non-profit usage, directly usable with Nexus and ESRF 2D data format., (n.d.).
- [29] M. Wojdyr, Fityk: a general-purpose peak fitting program, *J. Appl. Crystallogr.* 43 (2010) 1126–1128.
- [30] S. Stern, S. Trohalaki, *Fundamentals of Gas Diffusion in Rubbery and Glassy Polymers*, 1990.
- [31] A.D. French, Idealized powder diffraction patterns for cellulose polymorphs, *Cellulose* 21 (2014) 885–896.
- [32] C.N.C. Cellulforce, *Product Specification*, CelluForce, 2016, pp. 1–3. www.celluforce.com.
- [33] T. Messin, N. Follain, A. Guinault, C. Sollogoub, V. Gaucher, N. Delpouve, S. Marais, Structure and barrier properties of multilayered biodegradable PLA/PBSA films: confinement effect via forced assembly coextrusion, *ACS Appl. Mater. Interfaces* 9 (2017) 29101–29112.
- [34] U. Sonchaeng, F. Iniguez-Franco, R. Auras, S. Selke, M. Rubino, L.T. Lim, Poly(lactic acid) mass transfer properties, *Prog. Polym. Sci.* 86 (2018) 85–121.
- [35] H. Jadhav, A. Jadhav, P. Takkalkar, N. Hossain, S. Nizammudin, M. Zahoor, M. Jamal, N. Mubarak, G. Griffin, N. Kao, Potential of polylactide based nanocomposites-nanopolysaccharide filler for reinforcement purpose: a comprehensive review, *J. Polym. Res.* 27 (2020) 1–36.
- [36] N. Tenn, N. Follain, J.r.m. Soulestin, R.I. Crétois, S. Bourbigot, S.p. Marais, Effect of nanoclay hydration on barrier properties of PLA/montmorillonite based nanocomposites, *J. Phys. Chem. C* 117 (2013) 12117–12135.
- [37] S. Zid, M. Zinet, E. Espuche, Modeling diffusion mass transport in multiphase polymer systems for gas barrier applications: a review, *J. Polym. Sci. B Polym. Phys.* 56 (2018) 621–639.
- [38] L.E. Nielsen, Models for the permeability of filled polymer systems, *J. Macromol. Sci. Part A - Chemistry* 1 (1967) 929–942.
- [39] R.K. Bharadwaj, Modeling the barrier properties of polymer-layered silicate nanocomposites, *Macromolecules* 34 (2001) 9189–9192.
- [40] A. Bendahou, H. Kaddami, E. Espuche, F. Gouanvé, A. Dufresne, Synergism effect of montmorillonite and cellulose whiskers on the mechanical and barrier properties of natural rubber composites, *Macromol. Mater. Eng.* 296 (2011) 760–769.
- [41] S. Kanehashi, K. Nagai, Analysis of dual-mode model parameters for gas sorption in glassy polymers, *J. Membr. Sci.* 253 (2005) 117–138.
- [42] D. Sun, J. Zhou, Molecular simulation of oxygen sorption and diffusion in the poly(lactic acid), *Chin. J. Chem. Eng.* 21 (2013) 301–309.
- [43] S.A. Stern, S. Trohalaki, *Fundamentals of Gas Diffusion in Rubbery and Glassy Polymers, Barrier Polymers and Structures*, American Chemical Society 1990, pp. 22–59.
- [44] J. Wang, D.J. Gardner, N.M. Stark, D.W. Bousfield, M. Tajvidi, Z. Cai, Moisture and oxygen barrier properties of cellulose nanomaterial-based films, *ACS Sustain. Chem. Eng.* 6 (2018) 49–70.
- [45] M. Martínez-Sanz, A. Lopez-Rubio, J.M. Lagaron, High-barrier coated bacterial cellulose nanowhiskers films with reduced moisture sensitivity, *Carbohydr. Polym.* 98 (2013) 1072–1082.
- [46] C. Aulin, M. Gallstedt, T. Lindstrom, Oxygen and oil barrier properties of microfibrillated cellulose films and coatings, *Cellulose* 17 (2010) 559–574.
- [47] N. Kuananusont, U. Pongsa, A. Bunsiri, A. Somwangthanoj, Effect of relative humidity on oxygen permeability of modified poly(lactic acid) blown films, in: *Proceedings of Pure and Applied Chemistry International Conference*, Khon Kaen, 2014, pp. 630–633.
- [48] Y. Liu, L.M. Matuana, Surface texture and barrier performance of poly(lactic acid)-cellulose nanocrystal extruded-cast films, *J. Appl. Polym. Sci.* 136 (2019), 47594.
- [49] N. Tenn, N. Follain, K. Fatyeyeva, F. Poncin-Epaillard, C. Labrugère, S. Marais, Impact of hydrophobic plasma treatments on the barrier properties of poly(lactic acid) films, *RSC Adv.* 4 (2014) 5626–5637.
- [50] R. Koppolu, J. Lahti, T. Abitbol, A. Swerin, J. Kuusipalo, M. Toivakka, Continuous processing of nanocellulose and polylactic acid into multilayer barrier coatings, *ACS Appl. Mater. Interfaces* 11 (2019) 11920–11927.